Experimental observation of self-imaging in SMF-28 optical fibers

F. MANGINI,[1,*] **M. FERRARO,**[2] **M. ZITELLI,**[2] **A. NIANG,**[1] **A. TONELLO,**[3] **V. COUDERC,**[3] **O. SIDELNIKOV,**[4] **F. FREZZA,**[2] **AND S. WABNITZ**[2,4]

[1]*Department of Information Engineering (DII), University of Brescia, Via Branze 38, 25123 Brescia, Italy*
[2]*Department of Information Engineering, Electronics and Telecommunications (DIET), Sapienza University of Rome, Via Eudossiana 18, 00184 Rome, Italy*
[3]*Université de Limoges, XLIM, UMR CNRS 7252, 123 Avenue A. Thomas, 87060 Limoges, France*
[4]*Novosibirsk State University, Pirogova 1, Novosibirsk 630090, Russia*
*fabio.mangini@unibs.it

Abstract: Spatial self-imaging, consisting of the periodic replication of the optical transverse beam profile along the propagation direction, can be achieved in guided wave systems when all excited modes interfere in phase. We exploited material defects photoluminescence for directly visualizing self-imaging in a few-mode, nominal singlemode SMF-28 optical fiber. Visible luminescence was excited by intense femtosecond infrared pulses via multiphoton absorption processes. Our method permits us to determine the mode propagation constants and the cutoff wavelength of transverse fiber modes.

1. Introduction

Spatial self imaging (SSI) is a physical phenomenon consisting of the periodic replication, along the propagation distance, of the transverse spatial distribution of an electromagnetic field in the presence of diffraction. SSI was firstly observed in 1836 by Talbot, who showed that the image formed by the incidence of a plane wave on a diffraction grating is periodically replicated in free-space propagation [1]. More than one century later, SSI was conceived and demonstrated in slab waveguides [2,3], where the electromagnetic field is confined due to total internal reflection, and diffraction competes with index guiding, leading to guided modes. These results paved the way for the use of SSI in integrated optics, e.g., for developing highly efficient planar waveguide couplers [4].

SSI in waveguides results from the interference among their guided modes and, for this reason, it has been extensively investigated in multimode (MM) systems. When a given electromagnetic field is injected into a MM waveguide, it can be decomposed into a specific set of excited modes. Each mode propagates independently with its own propagation constant, and it interferes with other modes. Therefore, a replica of the input field can be obtained at specific positions along the waveguide, where all modes are in-phase. Mathematically, this is always possible, although the distance of the first self-imaging point grows larger as the number of excited modes increases.

This observation is independent of the system geometry, and it also applies to cylindrical waveguides, e.g. optical fibers. The first observation of SSI in multimode fibers (MMFs) was reported by Allison in 1994 [5]. Since then, many studies have been carried out, proposing MMFs for the development of sensing devices based on SSI. A basic structure of such devices consists of splicing singlemode – multimode – singlemode fibers [6,7]: depending on an external parameter, e.g. temperature, the beam at the interface between the input singlemode fiber (SMF) and the MMF may be imaged at the MMF output thanks to multimode interference. Besides sensors, SSI in MMFs has been proposed for many other applications, ranging from bandpass filters [8] to fiber lenses [9], fiber lasers, and amplifiers [10–12].

Although SSI in waveguides is a well-known linear propagation effect, only recently SSI could be directly measured, thanks to the presence of nonlinear effects induced by high peak-power ultrashort laser pulses. Specifically, by exploiting doped silica photoluminescence (PL), it has been shown that multiple photons can be simultaneously absorbed by an optical fiber, which produces a periodic array of visible side-scattered light spots at points of peak intensity [13–15].

As illustrated by these experiments [14], there is a significant difference between SSI in step-index (SI) and graded-index (GRIN) MMFs. In SI fibers, the mode propagation constants are not equispaced in the spatial frequency domain: as a result, the SSI distance is about a few centimeters long [10]. Conversely, for GRIN MMFs with a parabolic index profile, the propagation constants of nondegenerate mode groups are equally spaced. Therefore, in these fibers, the SSI length is as short as a few hundred microns [13,16].

In this work, we exploit the fiber defects PL in order to directly visualize the spatial intensity profiles resulting from the modal interference in a particular, and relevant for optical communications, type of SI fiber. Specifically, we consider an SMF-28 fiber operating in the few-mode regime, which permits to combine the presence of a core-cladding index discontinuity with a relatively short SSI distance.

As it is well known, the fiber cutoff wavelength [17] is defined as the wavelength $\lambda_c^{th} \simeq 2\pi a n_c \sqrt{2\Delta - \Delta^2}/2.405$, where n_c is the core refractive index, Δ is the core-cladding relative refractive index difference and a is the core radius [18]. For wavelengths $\lambda > \lambda_c^{th}$, only the fundamental mode is guided by the fiber. Whereas, when operating at $\lambda < \lambda_c^{th}$, it is possible to propagate several modes in an SMF-28. Nevertheless, in practical deployment conditions of an SMF-28 fiber, and particularly for telecom applications, such fiber effectively behaves as singlemode over an extended wavelength range, that is, for wavelengths above an effective cutoff (or nominal cutoff value provided by the fiber manufacturer) wavelength, say, $\lambda_{eff} < \lambda_c^{th}$. This is because environmental conditions such as cabling and micro- and macro-bending introduce higher losses for higher-order modes than for the fundamental, so that they are eventually lost.

On the other hand, perhaps less appreciated is the fact that, when very short (e.g., of the other of 1 cm) fiber samples are involved, also when $\lambda > \lambda_c^{th}$ higher-order leaky modes can be excited at the fiber input, and still be revealed at its output. This is simply because the fiber length is shorter than their attenuation distance [19]. Here, by employing a fiber sample which is shorter than the attenuation distance of the LP$_{11}$ mode, we experimentally measure a cutoff wavelength, say, λ_c^{exp} which is even larger than λ_c. Note also that, by properly acting on both the position and angle of incidence, the measured cutoff wavelength can be tuned, possibly widening the few-mode propagation regime of a SMF-28 [17]. Notably, by controlling the input coupling conditions one may excite meridional and skew rays [20,21], which enables the observation of SSI.

In our experiments, we report the observation of SSI at wavelengths up to 200 nm longer than the SMF-28 λ_{eff} value, when only a few microns offset of the input beam position is introduced. The SSI period is found to be independent of the input conditions such as the laser power and the coupling geometry. In this sense, our results provide a way to estimate the propagation constant of the modes, as well as a method to experimentally determine, by a proper adjustment of its length, the cutoff wavelength λ_c of a fiber. Measuring the mode propagation constants and λ_c is of utmost importance in telecom applications, in particular those involving few-mode fibers for spatial division multiplexing (SDM) transmissions [19,22–24]. Our method can also be applied to the study of modal noise in optical communication systems. In fact, a leaky LP$_{11}$ mode can be first excited in a fiber pigtail, and then coupled back to the fundamental LP$_{01}$ mode at a subsequent splice, leading to modal noise and performance degradation [19].

2. Theory

When considering linear beam propagation in an optical fiber, with no loss of generality, any electromagnetic field F, confined inside the core, can be decomposed as a superposition of guided

modes $\varphi_{lm}(r, \vartheta)$, as sketched in Fig. 1(a):

$$F(r, \vartheta, z) = \sum_{l,m} c_{lm} \varphi_{lm}(r, \vartheta) e^{-j\beta_{lm}z}, \tag{1}$$

where the sums run over all the (l, m) guided modes with propagation constant β_{lm}, and the series expansion coefficients $\{c_{lm}\}$ can be determined starting from the incident beam as follows [17]:

$$c_{lm} = \frac{\int \int F(r, \vartheta, z = 0)\varphi_{lm}(r, \vartheta)rdrd\vartheta}{\sqrt{\int \int |\varphi_{lm}(r, \vartheta)|^2 rdrd\vartheta}} \tag{2}$$

The SSI condition can be found by imposing $F(r, \vartheta, z_{SSI}) = F(r, \vartheta, 0)$, with z_{SSI} being the SSI distance. This reads:

$$(\beta_{01} - \beta_{lm})z_{SSI} = 2v_{l,m}\pi, \qquad \forall l, m \tag{3}$$

where $v_{l,m}$ are integer numbers. Clearly, the number of constraints expressed by (3), which are necessary to make all modes simultaneously interfering in-phase, increases with the variety of the involved β_{lm} values. Remarkable is the case of GRIN fibers, where the constructive interference condition for all modes is the same. Analogously, whenever the SMF-28 guides first two modes, the SSI condition boils down to $(\beta_{01} - \beta_{11})z_{SSI} = 2\pi$. In general, few-mode excitation can be obtained by introducing a small misalignment of the input beam with respect to the fiber axis.
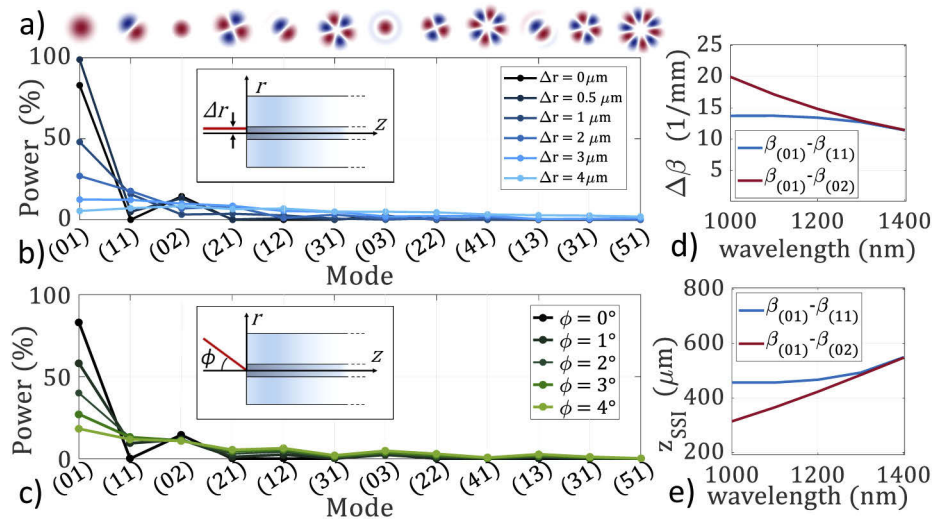
Fig. 1. a) Sketch of the spatial profile of the first 12 SMF-28 guided modes; b,c) Modal power distributions of an 8.3 μm wide Gaussian beam at the wavelength $\lambda = 1030$ nm, vs. position offset or tilt angle, as depicted in the inset; d,e) Propagation constant difference with respect to the fundamental mode, and corresponding SSI period values vs. input wavelength, calculated as in Eq. (3).

This can be seen in Figs. 1(b) and (c), where we illustrate how the mode power fraction $|c_{lm}|^2$ is affected when varying either the input position offset Δr, or the tilt angle ϕ, respectively, for an input Gaussian beam. Here the input beam at $\lambda = 1030$ nm has an 8.3 μm diameter at $1/e^2$ of peak intensity, and the fiber core diameter is 8.8 μm. Figures 1(b) and (c) shows that, if the input beam is perfectly aligned with the fiber axis, only radial modes (i.e. with $l = 0$) are excited. Conversely, when a symmetry-breaking misalignment is progressively introduced, additional modes emerge inside the core, and their power fraction tends to become uniform. If a relatively

small position offset is introduced between the input beam and the center of the SMF-28 core, only the $(l = 0, m = 1)$ mode has a non-negligible power fraction. It must be noted that, for $\Delta r > 0.8$ μm, the beam partially propagates inside the cladding, and the mode decomposition (1) no longer holds. One can always ideally compute the modal decomposition, as in Figs. 1(b) and (c), but in practical cases, only the two lowest modes survive during propagation.

A numerical mode solver was used to compute the propagation constants, as described in Ref. [25]. In Figs. 1(d) and (e) we show the wavelength dependence of $\Delta\beta = \beta_{01} - \beta_{lm}$ and z_{SSI}, respectively. As it can be seen, an SSI period of 456 μm owing to LP$_{01}$-LP$_{11}$ mode interference is expected, for wavelengths shorter than 1100 nm (blue curve). For a perfect alignment of the input beam, a second period smaller than 400 μm should also be observed (red curve) because of LP$_{01}$-LP$_{02}$ mode beating. However, as we shall see, this condition was never reached in our experiments: only the LP$_{01}$-LP$_{11}$ mode beating was detected.

3. Experimental results

The experimental setup used for the demonstration of SSI-induced PL in a few-mode fiber consists of an ultra-short pulse laser system, involving a hybrid optical parametric amplifier (OPA) of white-light continuum (Lightconversion Orpheus-F), pumped by a femtosecond Yb-based laser (Lightconversion Pharos-SP-HP). We set the laser wavelength at 1030 nm (when using Pharos pulses directly), or between 1200 nm and 1500 nm (when using idler pulses from the OPA). The laser beam was focused by a 19 mm lens into a 1 cm sample of 8.8/125 μm SMF-28 with a beam diameter of 8.3 μm at $1/e^2$ of peak intensity. The SMF-28 has a core refractive index of n_c=1.467, Δ=0.003 at 1030 nm, and $\lambda_c^{th} = 1305$ nm. The output beam was collected by a micro-lens of 8 μm focal distance, and sent to the analysis devices. Near- and far-field images of the output beam were measured with a calibrated and automated optical system (Gentec Beamage M4-IR); the beam power was measured by a thermopile power meter (GENTEC XLP12-3S-VP-INT-D0), spectra by a miniature fiber optics spectrometer (Ocean Optics USB2000+) with 170-1150 nm spectral range and an optical spectrum analyzer (OSA) (Yokogawa AQ6370D) with wavelength ranges of 700-1700 nm, respectively.

Our numerical model for simulating the SSI of ultrashort, high peak power pulses in few-mode fibers was based on solving the $(3D + 1)$ generalized nonlinear Schröedinger equation, involving a single field for each polarization, including all frequencies and modes. The nonlinear contributions taken into account in the model are: Kerr and Raman effects, self-steepening, third-harmonic generation, and an effective two-photon absorption to take into account losses due to the PL. The values of the second- and third-order dispersion parameters, the linear absorption coefficient and the nonlinear refractive index are $\beta_2 = 19.01$ ps^2/km and $\beta_3 = 0.038$ ps^3/km, $\alpha = 3.7 \times 10^{-4}$ 1/m, and $n_2 = 2.7 \times 10^{-20}$ m^2/W respectively. Further details and a full list of the parameters used in the simulation can be found in [26].

In our experiments, we exploited the PL of silica defects in order to directly measure SSI in a SMF-28. PL was generated by the multiphoton absorption of high peak power ultrashort infrared (IR) pulses [13,14]. We injected 60 fs pulses with 4.15 MW peak power and 100 kHz repetition rate at the 1300 nm carrier wavelength, which is above the effective cutoff value λ_{eff} provided by the manufacturer (1260 nm). We injected the laser beam into the fiber with a position offset $\Delta r = 2$ μm: the beam peak intensity at the SSI self-focusing points was high enough ($\sim 10^{12} W/cm^2$) to excite PL but not so high to damage the fiber, being the fluence damage threshold of the order of 10^{13} W/cm^2 in the infrared range [27]. Note that the length scale for the decay of the leaky $(l = 1, m = 1)$ mode that is excited by femtosecond pulses at telecom wavelengths is of the order of a few tens of centimeters [19], which is much longer than our sample length.

By means of a digital microscope, we captured images of light side-scattered out of the fiber. Figures 2(a) and (b) show the periodic PL trace, with room light switched on and off, respectively. We analyzed the Fourier content of the spatial evolution of the PL intensity profile, as shown in

Fig. 2(c). The fundamental harmonic, which covers more than 90% of the signal, has a periodicity $z_{PL} = 246$ μm. The solid line in Fig. 2(c) represents the sum of the first three harmonics that, besides the white scattering spots generated by fiber surface imperfections, fits well experimental data. In Fig. 2(d) we compare the periodic PL intensity evolution with the oscillating behavior of the simulated effective area of the beam. As it can be visually appreciated, there is a rather good agreement between experiments and simulations: the estimated periodicities differ by less than 1 μm. The PL periodicity (246 μm) is in good agreement with the theoretical expectation: half of the theoretical z_{SSI} (492 μm), since the PL depends on the beam intensity, while the SSI condition is on the electric field. So if one imposes the condition $|F(r, \vartheta, z_{SSI})|^2 = |F(r, \vartheta, 0)|^2$, two classes of solutions emerge: even and odd. Therefore, the PL appearance condition is $(\beta_{01} - \beta_{11})z_{PL} = \pi\nu$ (where ν is an integer number), which differs, as expected, by a factor 2 from the value given by Eq. (3).
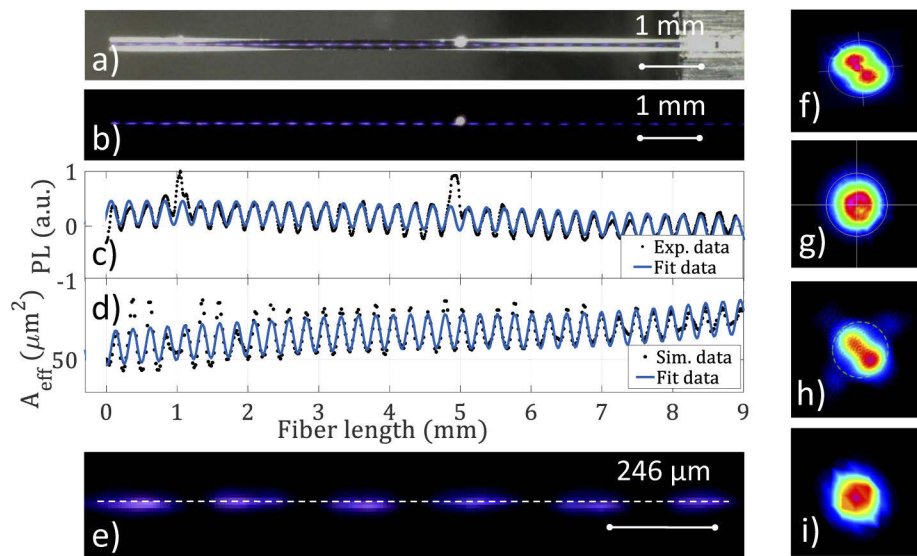
Fig. 2. a) Microscope image of a 1 cm long SMF-28, where SSI is visualized via defects PL. b) same image as a), with room light off c) Analysis of PL intensity evolution along the fiber. d) Evolution of numerically calculated effective area along the fiber. e) Zoom of b). f,g) Measured output near- and far-field transverse intensity profiles. h,i) Numerically calculated near- and far-field intensities.

Figure 2(e) is a zoom-in of Fig. 2(b), which makes appreciable the parity difference between z_{SSI} and z_{PL}. Finally, Figs. 2(f) and (g) shows experimental output near- and far-field intensity profiles, which are in good qualitative agreement with simulations, see Figs. 2(h) and (i). The fiber length used in the numerical simulations was determined through the digital microscope. We highlight that, despite nonlinear processes such as the multiphoton absorption are involved, the SSI periodicity is not impacted by nonlinear effects. We experimentally verified that the SSI period is not affected by beam intensity. In Fig. 3(a), we show PL images for several input peak powers. Here we traced vertical red dashed lines, in order to underline the constancy of the SSI period. Similarly, in Fig. 3(b) we report numerical simulations for a 5 mm long fiber, showing that the periodic oscillation of the beam effective area is barely modified by the input power. Nonlinear terms do play a role in the beam dynamics and consequently in the PL intensity. However, their contribution only acts on the field amplitude, without affecting SSI periodicity [13].
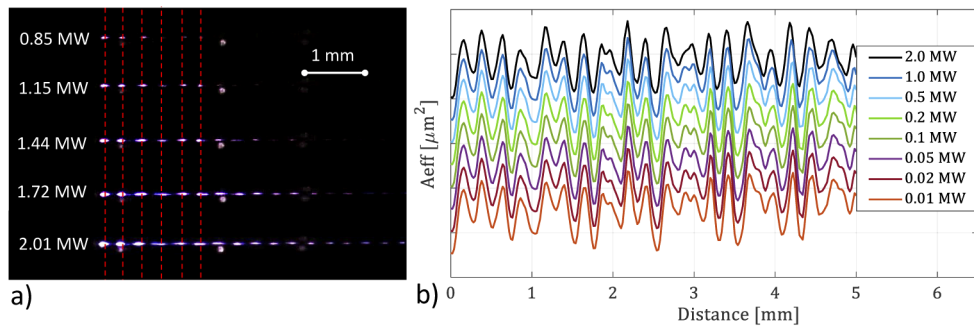
Fig. 3. a) Microscope image of PL from a 5 mm long SMF-28, when varying the input peak power. b) Numerical effective area modulation along propagation for different input peak powers. Curves are vertically offset, in order to make their difference more visible.

In order to further investigate SSI in the SMF-28, we varied the input beam misalignment when injecting 170 fs pulses with 1.35 MW peak power at a wavelength of 1030 nm. At such wavelength, the theoretically predicted value of the PL periodicity is 228 μm. In Fig. 4(a), we show that periodic PL emission along the entire SMF-28 sample length is generated for up to 5 μm of the input position offset, i.e., as long as the beam center is coupled inside the fiber core. On the other hand, the PL intensity becomes irregular when the beam mostly propagates in the cladding, and eventually only the first self-focusing point remains visible.
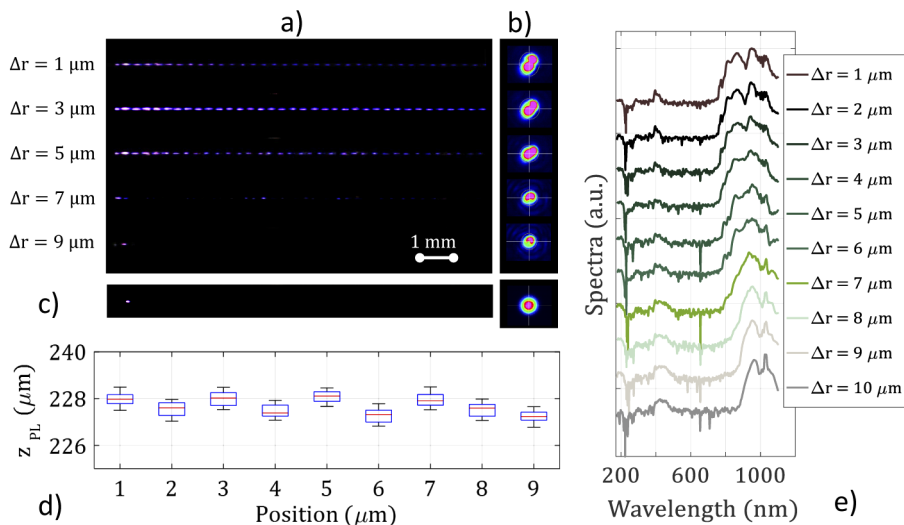

Fig. 4. a) Images of PL emission for different input beam offsets Δr; b) Corresponding near-field profiles; c) Same as a) and b), for a perfectly aligned beam with a diameter of 1.4 μm at 1.72 MW peak power; d) PL period vs. offset Δr. The standard deviation, identified by the blue boxes, was calculated starting from the distance between each couple of consecutive PL spots, while the red line represents the median. e) Output spectra for different values of Δr.

The output near-field beam intensity profiles corresponding to Fig. 4(a) are reported in Fig. 4(b), showing the excitation of higher-order modes, similarly to Figs. 2(f) and (h). For comparison, we also show in Fig. 4(c) the case of a perfectly aligned, and narrower (i.e., with input beam diameter of 1.4 μm) input beam: in this case, the output near-field has a Gaussian profile, and

PL only appears from a single emitting spot, due to the initial beam self-focusing. With such input beam conditions, it is apparent that only the fundamental mode propagates after 1 cm of fiber. We underline that obtaining such single-point PL emission is very sensitive to the input beam alignment: a little input position offset results in the same PL emission as in Fig. 4(a). PL periodicity values measured from the latter are reported in Fig. 4(d). This shows that the SSI period remains constant even when the position of the incoming beam is varied, meaning that only LP_{01} and LP_{11} mode beating contributes to SSI in all cases. Finally, in Fig. 4(e) we display the dependence of the output pulse spectra on input position offset, showing that nonlinear spectral broadening is mitigated as the fraction of power in the core is reduced.

Finally, we compared the theoretical (as given by Eq. (3)) and experimental wavelength dependence of the SSI periodicity, when the source wavelength was varied between 1030 nm and 1500 nm. We injected the laser beam into the fiber with a position offset $\Delta r = 4$ μm. All measurements were performed at 30 mW of average input power at 100 kHz of repetition rate (the pulse duration for the different wavelengths was 170 fs at 1030 nm and about 60 fs for the other wavelengths). The corresponding PL emission images are shown in Fig. 5(a), revealing that the PL color changes as the source wavelength is varied, because of the excitation of different types of material defects. Specifically, a contribution from Oxygen-Deficiency-Centers provides blue/violet colored emission; whereas Non-Bridging-Oxygen-Hole-Centres are responsible for the emission of red PL [14,28]. In Fig. 5(a), we underline the position of the PL intensity peaks at 1030 nm by drawing vertical white dashed lines. As it can be seen, when the wavelength reaches a threshold value, above 1450 nm, PL appears as a single point, similarly to the case in Fig. 4(c). This is the hallmark of pure singlemode propagation, that defines the cutoff wavelength λ_c^{exp}.
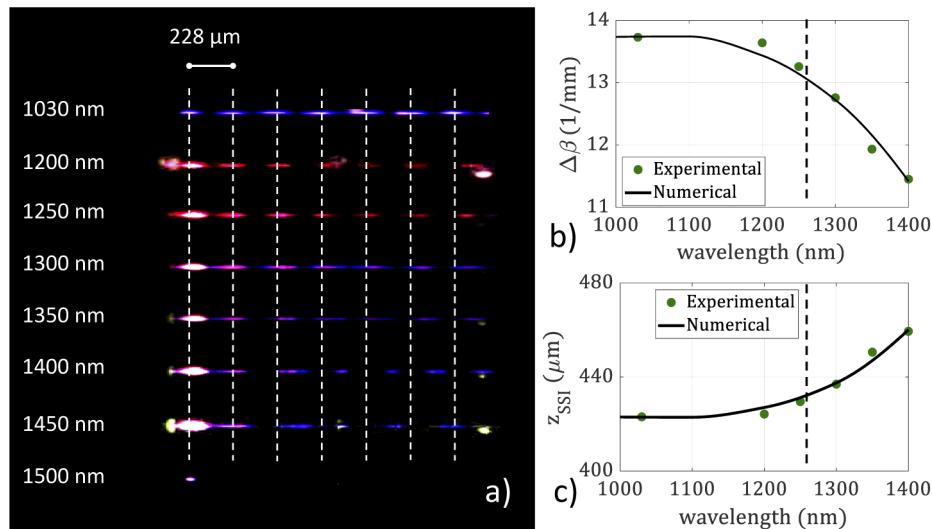
Fig. 5. a) Microscope images of silica defects PL when varying the input pulses wavelength. Dashed vertical white lines mark the PL periodicity at 1030 nm. b) and c) Comparison between experimental and theoretical values of $\Delta\beta = \beta_{01} - \beta_{11}$ and of the SSI period (same as in the blue curve in Fig. 1(d) and Fig. 1(e)), respectively. The parameters are the same as in Fig. 2, but the input peak power is set to 1.72 MW.

In Figs. 5(b) and (c) we draw the comparison between measured and theoretical values of $\Delta\beta = \beta_{01} - \beta_{11}$ and of the SSI period, respectively. The dashed vertical line indicates the manufacturer provided effective cutoff wavelength λ_{eff}=1260 nm, which is about 200 nm shorter than our experimentally determined cutoff wavelength λ_c^{exp}=1450 nm. This value is 145 nm higher than the theoretical value (λ_c=1305 nm). As previously discussed, for the used short fiber

length the higher-order leaky mode is not attenuated yet. By decreasing the input beam offset, the power fraction of excited higher-order modes tends to decrease (see Fig. 1(b)), so that the cutoff λ_c^{exp}, as determined via SSI, is expected to approach the theoretical value λ_c^{th}. From Fig. 5(b), we may note that our method permits to determine the difference between the propagation constants of higher-order modes. In particular, once that the LP_{01} propagation constant is known, it is possible to determine the propagation constant of the LP_{11} mode. Furthermore, by knowing that $2\pi/\Delta\beta = \lambda/\Delta n_{eff}$, the effective refractive index of the LP_{11} mode also can be determined.

4. Conclusion

In conclusion, we experimentally characterized SSI in a two-mode fiber (SMF-28 or nominal SMF), by means of PL induced by the silica defects multiphoton absorption of intense near-IR femtosecond pulses. As a result of SSI-induced periodic beam focusing, the use of femtosecond pulses permits to reach intensity levels that are high enough to trigger multiphoton absorption, which generates visible luminescence at an array of emitting spots, detectable by the naked eye. This makes it possible to carry out a direct measurement of the SSI periodicity, in contrast to indirect, modal temporal autocorrelation measurements [19].

Few-mode propagation, with the associated SSI beating, was obtained for pulse wavelengths both below and above the theoretical cutoff value. The excitation of the LP_{01} and LP_{11} modes with comparable power fraction was induced by means of a misalignment between the incident beam and the fiber axis. Our measurements determined that the SSI period is robust with respect to the input beam position offset, which greatly facilitates its observation. Experiments and theoretical predictions were found to be in excellent agreement. Furthermore, we demonstrated that the manifestation of SSI is qualitatively consistent with the complex nonlinear beam dynamics, that is simulated by means of a 3D+1 generalized nonlinear Schrödinger equation.

The use of PL emission in order to visualize SSI permitted us to accurately estimate the range of effective bimodal propagation of a short fiber sample. In perspective, we believe that our results could find applications to few-mode fibers for SDM, by providing a simple and yet powerful tool to determine their propagation constants via the direct measurement of the SSI period.

Data availability. Data underlying the results presented in this paper are not publicly available at this time but may be obtained from the authors upon reasonable request.

References

1. H. Talbot, "LXXVI. Facts relating to optical science. No. IV," The London, Edinburgh, Dublin Philos. Mag. J. Sci. **9**(56), 401–407 (1836).
2. O. Bryngdahl, "Image formation using self-imaging techniques," J. Opt. Soc. Am. **63**(4), 416–419 (1973).
3. R. Ulrich and G. Ankele, "Self-imaging in homogeneous planar optical waveguides," Appl. Phys. Lett. **27**(6), 337–339 (1975).
4. L. B. Soldano and E. C. Pennings, "Optical multi-mode interference devices based on self-imaging: principles and applications," J. Lightwave Technol. **13**(4), 615–627 (1995).
5. S. Allison and G. Gillies, "Observations of and applications for self-imaging in optical fibers," Appl. Opt. **33**(10), 1802–1805 (1994).
6. A. H. Morshed, "Self-imaging in single mode-multimode-single mode optical fiber sensors," in *2011 Saudi International Electronics, Communications and Photonics Conference (SIECPC)*, (IEEE, 2011), pp. 1–5.
7. X. Wang, E. Lewis, and P. Wang, "Investigation of the self-imaging position of a singlemode-multimode-singlemode optical fiber structure," Microw. Opt. Technol. Lett. **59**(7), 1645–1651 (2017).

8. W. S. Mohammed, P. W. Smith, and X. Gu, "All-fiber multimode interference bandpass filter," Opt. Lett. **31**(17), 2547–2549 (2006).

9. W. S. Mohammed, A. Mehta, and E. G. Johnson, "Wavelength tunable fiber lens based on multimode interference," J. Lightwave Technol. **22**(2), 469–477 (2004).

10. X. Zhu, A. Schülzgen, H. Li, L. Li, L. Han, J. V. Moloney, and N. Peyghambarian, "Detailed investigation of self-imaging in largecore multimode optical fibers for application in fiber lasers and amplifiers," Opt. Express **16**(21), 16632–16645 (2008).

11. X. Zhu, A. Schülzgen, H. Li, L. Li, Q. Wang, S. Suzuki, V. L. Temyanko, J. V. Moloney, and N. Peyghambarian, "Single-transverse-mode output from a fiber laser based on multimode interference," Opt. Lett. **33**(9), 908–910 (2008).

12. R. Selvas, I. Torres-Gomez, A. Martinez-Rios, J. A. Alvarez-Chavez, D. May-Arrioja, P. LiKamWa, A. Mehta, and E. Johnson, "Wavelength tuning of fiber lasers using multimode interference effects," Opt. Express **13**(23), 9439–9445 (2005).

13. T. Hansson, A. Tonello, T. Mansuryan, F. Mangini, M. Zitelli, M. Ferraro, A. Niang, R. Crescenzi, S. Wabnitz, and V. Couderc, "Nonlinear beam self-imaging and self-focusing dynamics in a GRIN multimode optical fiber: theory and experiments," Opt. Express **28**(16), 24005–24021 (2020).

14. F. Mangini, M. Ferraro, M. Zitelli, A. Niang, A. Tonello, V. Couderc, and S. Wabnitz, "Multiphoton-absorption-excited up-conversion luminescence in optical fibers," Phys. Rev. Appl. **14**(5), 054063 (2020).

15. B. Chen, Q. Bao, and L. Tong, "Direct observation of multimode interference in rare-earth doped micro/nanofibers," Opt. Express **27**(19), 26728–26737 (2019).

16. G. P. Agrawal, "Invite paper: Self-imaging in multimode graded-index fibers and its impact on the nonlinear phenomena," Opt. Fiber Technol. **50**, 309–316 (2019).

17. A. W. Snyder and J. Love, *Optical waveguide theory* (Springer Science & Business Media, 2012).

18. G. P. Agrawal, *Nonlinear fiber optics* (Third edition, Par. 2.3, Academic Pre, 2001).

19. I. Cristiani, L. Tartara, G. P. Banfi, and V. Degiorgio, "Ultrashort-pulse investigation of the propagation properties of the lp 11 mode in 1.55-μm communication fibers," Opt. Lett. **26**(22), 1758–1760 (2001).

20. D. Kumar and P. K. Choudhury, "Introduction to modes and their designation in circular and elliptical fibers," Am. J. Phys. **75**(6), 546–551 (2007).

21. A. Cardama and E. Kornhauser, "Modal analysis of coupling problems in optical fibers," IEEE Trans. Microwave Theory Tech. **23**(1), 162–169 (1975).

22. K. Van Leeuwen and H. Nijnuis, "Measurement of higher-order mode attenuation in single-mode fibers: effective cutoff wavelength," Opt. Lett. **9**(6), 252–254 (1984).

23. L. Wei, R. Lowe, and C. Saravanos, "Practical upper limits to cutoff wavelength for different single-mode fiber designs," J. Lightwave Technol. **5**(9), 1147–1155 (1987).

24. D. Bayuwati, T. Waluyo, and I. Mulyanto, "Determination of the effective cut-off wavelength of several single-mode fiber patchcords," J. Phys.: Conf. Ser. **985**, 012002 (2018).

25. L. G. Wright, Z. M. Ziegler, P. M. Lushnikov, Z. Zhu, M. A. Eftekhar, D. N. Christodoulides, and F. W. Wise, "Multimode nonlinear fiber optics: Massively parallel numerical solver, tutorial, and outlook," IEEE J. Sel. Top. Quantum Electron. **24**(3), 1–16 (2018).

26. M. Zitelli, F. Mangini, M. Ferraro, A. Niang, D. Kharenko, and S. Wabnitz, "High-energy soliton fission dynamics in multimode GRIN fiber," Opt. Express **28**(14), 20473–20488 (2020).

27. C. W. Smelser, S. J. Mihailov, and D. Grobnic, "Hydrogen loading for fiber grating writing with a femtosecond laser and a phase mask," Opt. Lett. **29**(18), 2127–2129 (2004).

28. S. Girard, A. Alessi, N. Richard, L. Martin-Samos, V. De Michele, L. Giacomazzi, S. Agnello, D. D. Francesca, A. Morana, B. Winkler, I. Reghioua, P. Paillet, M. Cannas, T. Robin, A. Boukenter, and Y. Ouerdane, "Overview of radiation induced point defects in silica-based optical fibers," Rev. Phys. **4**, 100032 (2019).